

© 2019 IEEE. Personal use of this material is permitted. Permission from IEEE must be obtained for all other uses, in any current or future media, including reprinting/republishing this material for advertising or promotional purposes, creating new collective works, for resale or redistribution to servers or lists, or reuse of any copyrighted component of this work in other works.

This paper has been accepted for publication by

IEEE Transactions on Power Electronics.

DOI

10.1109/TPEL.2019.2932178

Citation

G. Zulauf and J. Rivas-Davila, "Single-Turn Air-Core Coils for High-Frequency Inductive Wireless Power Transfer," *IEEE Trans. Power Electronics*, in press.

IEEE Xplore URL

<https://ieeexplore.ieee.org/document/8782649>

More papers from Juan Rivas's group at Stanford University can be found here:

<http://superlab.stanford.edu/publications.html>

Single-Turn Air-Core Coils for High-Frequency Inductive Wireless Power Transfer

Grayson Zulauf, *Student Member, IEEE* and Juan M. Rivas-Davila, *Senior Member, IEEE*

Abstract—The efficiency of MHz-frequency inductive wireless power transfer designs is currently limited by the quality factor of the resonant tanks and the coils. In this work, we use two-dimensional finite element analysis to optimize the cross-section of single-turn air-core inductors for this application, and demonstrate coils for wireless power at the high-frequency and very-high-frequency ISM bands.

Our resonant tanks achieve diameter-normalized quality factors (Q_d) that are at least 25% better than the state-of-the-art for air-core coils at the 6.78 MHz ($Q_d = 73 \text{ cm}^{-1}$), 13.56 MHz (102), 27.12 MHz (123) and 40.68 MHz (137) industrial, scientific, and medical (ISM) bands. We highlight the importance of capacitor selection and the tank configuration for designing high-Q resonant tanks, and recover the increase of Q with frequency that is missing from existing literature. Further, we show that maximizing height is not ideal for wireless power transfer applications, and build high-performance coils at small heights.

We integrate these coils into a wireless power transfer system at 6.78 MHz and 500 W output power, showcasing a maximum DC-DC efficiency above 89% with a gap (3 cm) equal to the coil radius, a significant efficiency improvement over existing work.

I. INTRODUCTION

Inductive wireless power transfer (WPT), where energy is transferred across an air gap using a magnetic field, is gaining commercial adoption for consumer devices [1], electric vehicles [2], and a host of other applications, from implanted medical devices [3] to electric wheelchairs [4]. At frequencies in the hundreds of kHz, send and receive coils are constructed using litz wire, to mitigate the increase of conduction losses with frequency, and a magnetic ferrite, which provides field shaping. At MHz frequencies, solid wires are typically used, as achievable litz wire strand diameters are no longer effective [5] and suitable magnetic materials are difficult to find commercially [6]. These windings are combined in a series (S) or parallel (P) configuration to form the resonant network that enables high-frequency, efficient inductive power transfer, and the quality factor of this tank (Q_T) is the critical factor (in combination with the coupling factor, k) in determining the efficiency of the wireless link [7]–[9].

Refs. [7], [10] utilize two figure-of-merits (FOMs) for wireless links: the first FOM [7] uses the kQ product (similar

This work was supported in part by Cadence Design Systems through a Stanford Graduate Fellowship, in part by the National Science Foundation Graduate Fellowship, in part by a seed grant through Stanford's Precourt Institute for Energy, in part by Stanford's SystemX Alliance, and in part by the TomKat Center for Sustainable Energy.

G. Zulauf and J.M. Rivas-Davila are with the Department of Electrical Engineering, Stanford University, 420 Via Palou Mall, Stanford, CA, 94305 (email:gzulauf@stanford.edu).

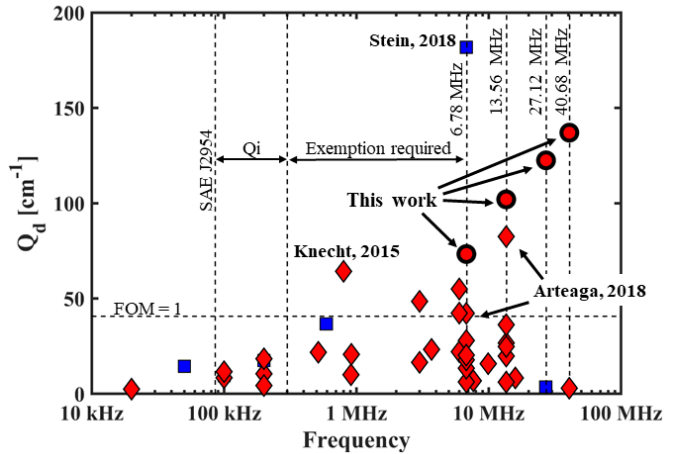


Fig. 1: Comparison between this work and the state-of-the-art in coils demonstrated in inductive WPT systems. Red-fill ‘♦’ (existing literature) and ‘●’ (this work) indicate air-core designs and blue-fill ‘■’ indicates designs using magnetic materials [3], [8], [9], [14]–[45]. We plot the minimum of Q_L and Q_T if both are provided. FOM = 1 is simulated performance for a loop of wire from [7]. Only the highest Q_d design at each ISM band from this work is shown.

to [8], [11], [12]) to compare published WPT coil performance to that of a single solid core wire, and the second [10] divides the coil quality factor (Q_L) by the diameter of the coil (d) for the normalized quality factor, Q_d . These FOMs assume that inductor losses dominate the losses in the resonant tank (as do most other WPT coil studies, e.g. [13]). At high voltages and MHz frequencies, however, selecting a low-loss resonant capacitor is non-trivial, and the quality factor of the constructed resonant tank (Q_T) should be used to determine efficiency to include other non-idealities beyond a lossy capacitor, such as solder joints and litz terminations.

These previous studies highlight an uncomfortable reality in high-frequency wireless power transfer: the design of the coils and, more broadly, the resonant tanks, are holding back achievable efficiencies. With the exception of the self-resonant structure in the same paper, Ref. [10] finds a maximum Q_d in the literature of 28 cm^{-1} near the 6.78 MHz International, Scientific, and Medical (ISM) band. Even more worrying, [7] finds that nearly all reported designs perform worse than a loop of solid wire, which likely indicates either poor winding designs or resonators where the losses are dominated by the capacitors or interconnections. Recent papers with optimized

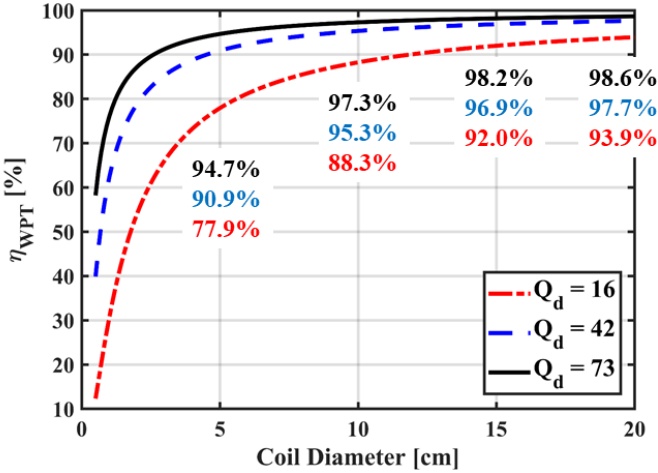


Fig. 2: Comparison between this work and coil state-of-the-art in maximum WPT efficiency (calculated using Eqn. 1) at a coupling of $k = 0.1$, which is a gap of about the coil radius [7], [10], [11], [19]. Efficiencies are marked at 5, 10, 15, and 20 cm coil diameters for each Q_d . Q_d of 16 is from a recent 6.78 MHz, air-core coil design paper [19], Q_d of 42 is the maximum found in the literature for air-core 6.78 MHz coils [36], and Q_d of 73 is measured here.

designs report a Q_d of 16.4 cm^{-1} for a 10 cm diameter coil, representing 96% of the total DC-DC WPT system losses in the paper [19]. In an extended survey of WPT coils (Figure 1), we find a maximum Q_d at the 6.78 MHz band of 42 cm^{-1} [36], and the same design achieves a Q_d of 82 at 13.56 MHz. From our survey, these can be considered the state-of-the-art in air-core coil design for WPT applications. Their design approach utilizes multiple turns of copper pipe, with the electrical length of the coil selected to balance conduction and radiation losses [11], [39], [42], and achieves Q_d very near the simulated Q for a simple loop of wire [7] at 6.78 MHz. This approach is difficult to scale for large coils ($> 50 \text{ cm}$) at MHz frequencies as the coil becomes limited to a single turn to keep the electrical length below a quarter wavelength.

In the 1 MHz frequency ballpark, existing coil performance factors are better [3], [20], but these operating frequencies fall between the Qi standard [1] and the 6.78 MHz ISM band, requiring an exemption to operate with open radiators. We also note that, unlike standard inductors, we do not observe the expected $\sqrt{\omega}$ increase of Q with higher operating frequencies. Taken together, air-core coils are limiting the efficiency of MHz-frequency wireless links across the literature, and most ferrite designs (excepting [10]) do not appear much better.

More explicitly, the efficiency of a loosely-coupled wireless link is [7], [13], [46], [47] (assuming equal transmit and receive tank quality factors, Q_T):

$$\eta = \frac{(kQ_T)^2}{\left(1 + \sqrt{1 + (kQ_T)^2}\right)^2}. \quad (1)$$

Under the assumptions of zero capacitor losses and a coupling coefficient of $k = 0.1$, which is close to an air

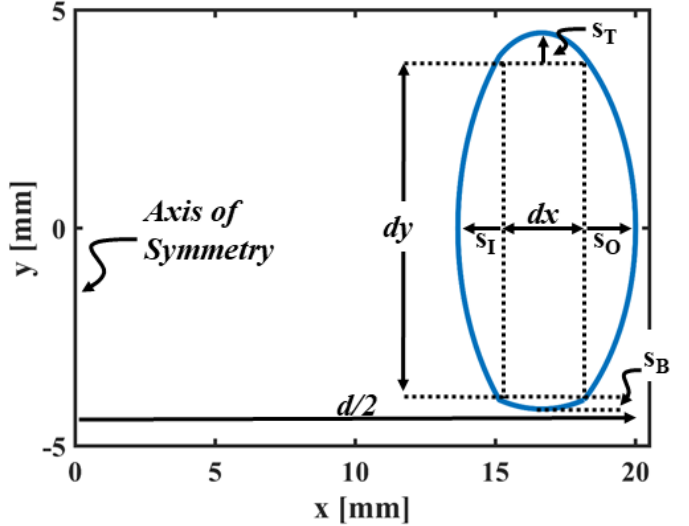


Fig. 3: Cross-section of WPT coil for coil optimization, with key parameters labeled. Simulation is two-dimensional and axisymmetric.

gap equal to the coil radius [7], [10], [11], [19], we plot the efficiency of the wireless link with coil diameter in Figure 2 (with coil quality factor scaled with diameter as $Q_L = Q_d \times d$). Using the state-of-the-art air-core Q_d of 42, we would need a nearly 10 cm coil to achieve over 95% efficiency (for a 5 cm gap), even without considering inverter, rectifier, or resonant capacitor losses!

Figures 1 and 2 highlight the potential for improved coil designs to significantly improve WPT systems at MHz frequencies. Certain applications in this space will prefer a ferrite-less design, especially those motivated by the reduced weight promised by high-frequency power electronics [48] (such as drones) or those operating in ruggedized or sensitive environments (e.g. implanted medical devices [3] or high-temperature applications). An improvement is even more urgent for small coils, as shown in Figure 2, where theoretical Q scales down linearly with diameter [7].

In this paper, we use finite element magnetostatic simulations to optimize single-turn air-core coil designs for loosely-coupled, MHz-frequency, inductive WPT, and build resonant tanks for a variety of coils to characterize the overall wireless link performance (Section II). In Section III, we discuss the extensibility of the optimization with changing coil diameter and height (III-A), operating frequency (III-B), air gap (III-C), and parallel and series resonant configurations (III-D). In Section IV, we demonstrate these coils in a 6.78 MHz, 500 W wireless power system to verify that the measured performance gains are maintained under large-signal conditions.

II. OPTIMIZATION PROCEDURE AND RESULTS

A. Procedure

For wireless power transfer systems, the key system specifications are coil diameter (d) and the distance between coils (g), and these two parameters are fixed for the optimization. Critically, the gap is defined as the distance between the closest

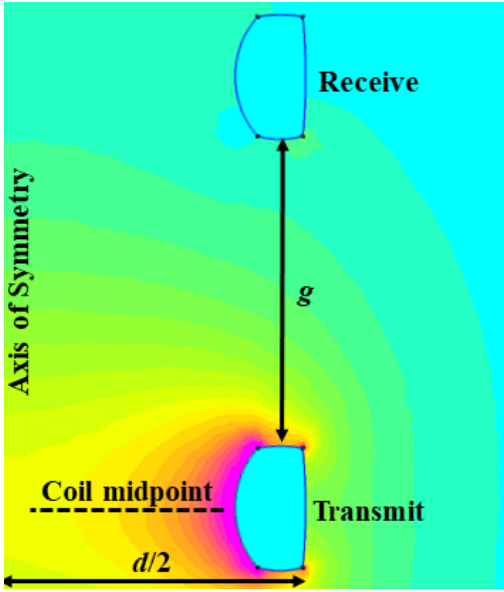


Fig. 4: FEMM simulation example for optimization, with current i in transmit coil and magnetic field strength $|H|$ shown in background.

parts of the coils, not the coil’s midpoint (as is done in some of the existing literature but discounts the effect of coil height). No part of the coil is allowed to exceed the specified diameter.

Six parameters are optimized, as shown in Figure 3:

- dx , the horizontal distance between the corner points,
- dy , the vertical distance between the corner points,
- s_O , the sagitta of the outer wall,
- s_I , the sagitta of the inner wall,
- s_T , the sagitta of the top wall, and
- s_B , the sagitta of the bottom wall.

The 2-D, axisymmetric, magnetostatic analysis is implemented using Finite Element Method Magnetics’s (FEMM) Lua interface [49]. We separate two symmetric coils by g , apply i current in the transmitting coil, and calculate the Q of the transmitting coil and k for the coupled pair. This optimization is shown in Figure 4. During WPT operation, i flows in the transmitting coil and a current (dependent on the coupling, self-inductance, and load resistance) flows in the receiving coil, which changes the magnetic field slightly relative to the simulated case. Under loose coupling, the focus of this work, this change in field is small in the vicinity of the transmitting coil. For speedy optimization, we ignore this change, and are therefore able to calculate both k and Q with a single simulation. The coil pair is symmetric in both geometry and orientation to further constrain the design space.

We begin with Matlab’s GlobalSearch algorithm to evaluate a broad range of shapes. GlobalSearch uses a local optimization in multiple starting basins [50] to minimize a cost function, which we define as $1/kQ$. This figure-of-merit kQ_d , which normalizes kQ for diameter (reported in cm^{-1}) better predicts WPT efficiency than a simple Q (or Q_d) optimization, as we detail later. kQ_d can compare different designs with a fixed gap-to-diameter ratio, and is a simpler-but-less-extensible version of the FOM in [7].

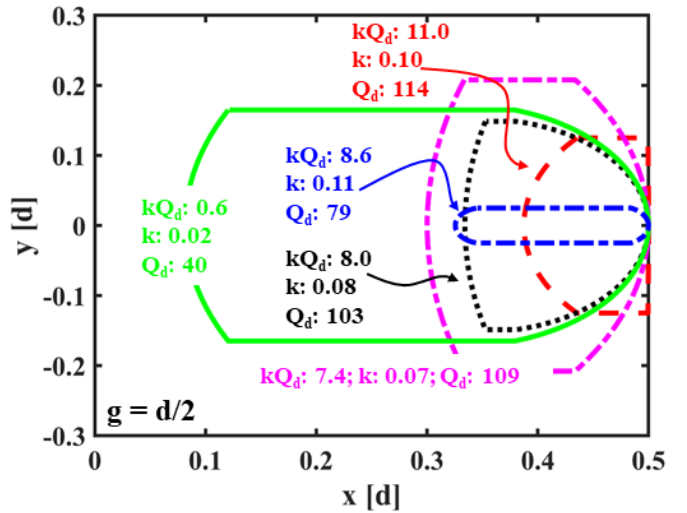


Fig. 5: Optimal bin cross-sections from a selection of GlobalSearch starting points, normalized for coil diameter (d). Frequency is 6.78 MHz and $g = d/2$. Simulated performance shown for each cross-section with $d = 1 \text{ cm}$.

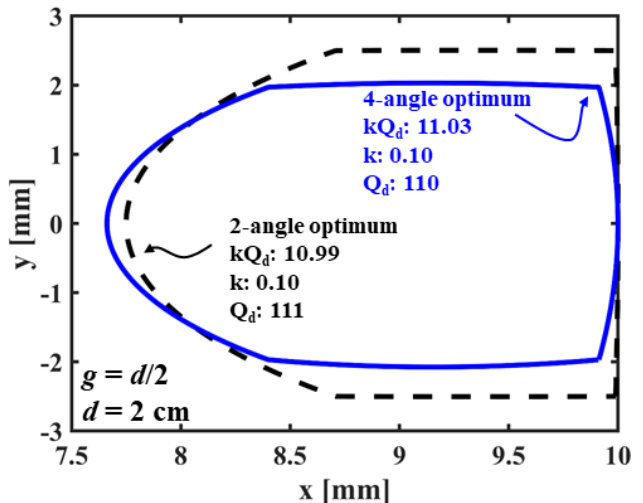


Fig. 6: Optimum cross-sections for 2 cm d coils with $g = d/2$. 4-angle optimum outperforms 2-angle optimum by 0.4% with a lower profile.

GlobalSearch returns the cost minimizer for each starting basin, identifying promising bins of designs to explore. We use these results to reduce the design space so that a simulation of a dense matrix of design points is feasible. Figure 5 shows a sampling of optimal configurations (2-angle optimization) for different starting basins, highlighting coil shapes and their expected performance. It is clear that some kind of optimization is paramount to achieve a good design – there is a nearly $3\times$ difference between two basin optimums in Q and more than an $18\times$ improvement in kQ . This optimization separates the work here from prior art that also used 3-D printing, but for inductor optimization [51], [52]. Fig. 5 shows that the shape *must* be optimized explicitly for a wireless power application, not solely on the basis of high- Q .

Our base optimization uses a frequency of 6.78 MHz, a

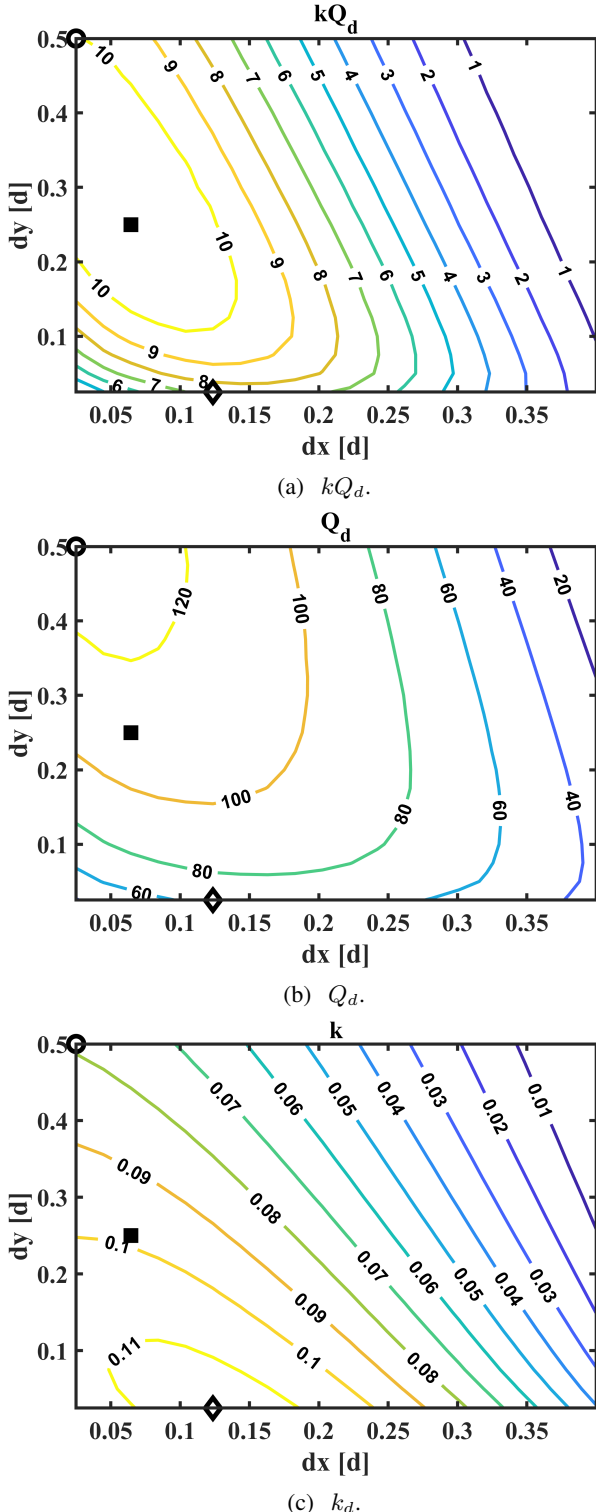


Fig. 7: Contour plots showing key figures-of-merit for 2-angle optimization results for $d = 2$ cm, $g = 1$ cm, $f = 6.78$ MHz, $s_I = 0.96$ mm (84°), $s_O = s_T = s_B = 0$. ‘■’ shows maximum kQ_d on each plot, ‘○’ shows maximum Q_d on each plot, and ‘◇’ shows maximum k on each plot.

copper thickness of 1.25 skin depths (1.25 δ), and a gap equal to the radius of the coil ($d/2$). The effect of these parameters on the optimized results are discussed in Section III. We

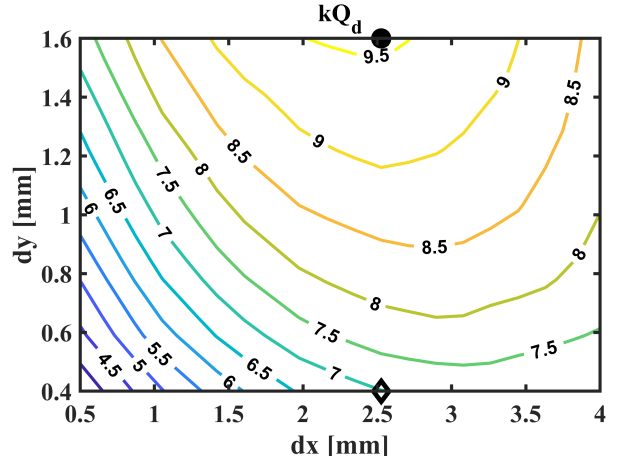


Fig. 8: Contour kQ_d plot for PCB height 2-angle optimization results for $d = 2$ cm, $g = 1$ cm, $f = 6.78$ MHz, $s_I = 0.43$ mm (114°), $s_O = s_T = s_B = 0$. ‘■’ shows maximum kQ_d and ‘○’ shows maximum Q_d (overlapped here), and ‘◇’ shows maximum k .

perform two GlobalSearch optimizations: one with flat top and bottom ($s_T = s_B = 0$), which we refer to as a *2-angle optimization*, and one with curvature on all four sides, or a *4-angle optimization*.

B. Optimization Results

The optimal shapes for the 2-angle and 4-angle optimization at $d = 2$ cm are shown in Figure 6. The optimal 4-angle cross-section has a large inner angle (large s_I) and small s_T , s_B , and s_O values. This can be explained by considering the tradeoffs with each angle. Under the constraint that the entire coil must be less than the diameter, a non-zero outer angle (s_O) effectively reduces the diameter of the coil by s_O . Similarly, with the coil configuration shown in Figure 4, where the gap (g) is the distance between the closest parts of the coils, non-zero s_T and s_B values increase the gap by the same amount. The inner angle has no such tradeoffs, and can therefore be aligned parallel to the magnetic field lines.

The 4-angle optimization improves upon the 2-angle optimization by 0.4% with a slightly smaller coil height. This minor improvement, while desirable, has the downsides of including three extra variables to optimize (s_O , s_T , and s_B). We fabricate two four-angle optimized coils but move forward with a deeper investigation of only the two-angle optimization.

For the 2-angle optimization, the fully-simulated design space is an inner angle varying from 0° to 180° (1° steps), dx from 2.5% to 40% of d (2.5% steps), and dy from 2.5% to 50% of d (2.5% steps). In the GlobalSearch 2-angle optimization, s_O is optimized, but for all designs, it is preferred to have a flat outer wall ($s_O = 0$), and we can eliminate this variable from the fully-simulated design space.

Figure 7 shows the optimization results for the refined simulation space for $d = 2$ cm coils and $g = d/2$. The optimal design point is a flat outer wall ($s_O = 0$), an inner angle of 84° (s_I is 4.8% of d), dx equal to 6.4% of d , and $dy = d/4$, which achieves a simulated kQ_d product of 11 cm^{-1} at 6.78 MHz

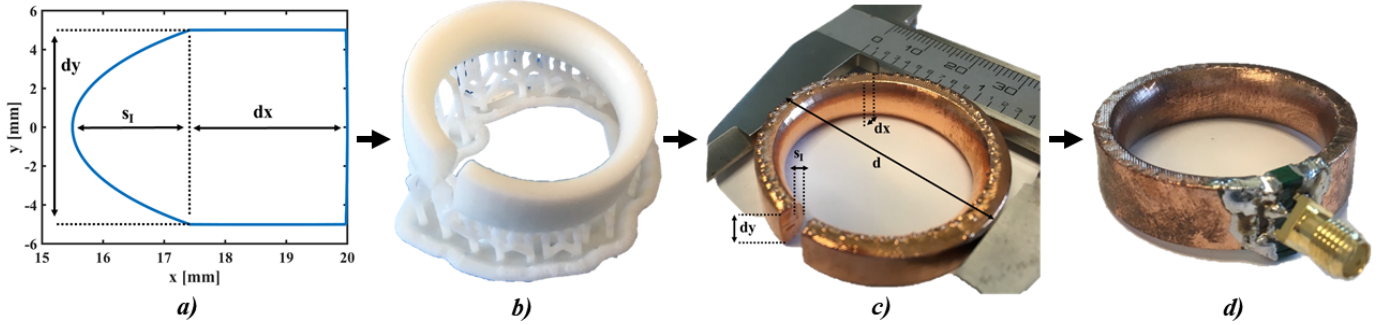


Fig. 9: Process implementation for construction of 2-angle optimization, 4 cm coil. *a)* shows cross-section for rotational extrusion, *b)* shows the 3-D printed coil with supports, *c)* shows the copper plated coil with annotations of the key parameters, and *d)* shows the plated coils with resonant capacitors.

and $g = d/2$. Q_d is 111 cm^{-1} at the maximized kQ_d point. This optimum is extensible across diameter and may be scaled up or down with the appropriate ratios.

Fundamentally, the optimum coil cross-section seeks to align the curvature of the copper with the curvature of the magnetic field, reducing impinging fields that cause current crowding. The curvature of the inner wall achieves this goal without compromise, but increasing coil height, which maximizes Q , is in tension with the constraints of achieving high k . Taller coils benefit Q at the expense of k and vice-versa, as increasing height improves inductor Q [51] but k decreases with larger coil height because the distance between the magnetic dipole moments near the vertical center-line of the coils increases (see Fig. 4). This height tradeoff indicates that *a)* our designs will not achieve the maximum Q_d possible, but should perform better in WPT systems and *b)* reducing the coil height, generally a desirable integration feature, will only degrade system performance by 10-20% (down to around $dy = 0.075d$) even though Q is significantly lower than its achievable maximum.

This small degradation at low height can be further mitigated with a reoptimization under a strict height constraint. A fair comparison might be a height comparable to a printed circuit board (PCB), the implementation for many spiral or single-turn inductors in the literature review of Figure 1. We reoptimize the coil geometry at 2 cm and 6 cm d for a standard PCB height of 1.6 mm, and find a preference for steeper inner angles to better align the inside copper with the magnetic field. The 2 cm optimization results are shown in Figure 8. At 2 cm d and 1.6 mm height, the kQ degradation is under 13% from an unlimited maximum height. At larger diameters, the coil performance degrades more for small heights, with low overall Q_d and large dx values decreasing the coupling coefficient. This coil could be easily implemented on a PCB with a standard height of 1.6 mm, a copper plating thickness of 1 oz ($35 \mu\text{m}$) or 2 oz ($70 \mu\text{m}$), and a dense array of vias to form the inner and outer walls, with kQ decreasing only 0.5% from switching from the optimized 114° angle to a 90° inner angle at $d = 2 \text{ cm}$.

The optimal design has a small dx value, and increasing the width of the coil monotonically reduces the efficiency of the coils. For comparison, an optimized toroidal inductor has dx

$(r_o - r_i)$ of around 37.5% of d [51], [53], so the optimized dx is again unique to the single-turn WPT application. Increasing dx degrades k significantly because the effective coil diameter is the average of the area of current flow, or, assuming evenly distributed current across the coil, $d - 2dx$. A single-turn coil with small dx , therefore, will have near-optimized coupling for both perfect alignment and misalignment conditions, as the current is concentrated very near the outer diameter.

Finally, we observe a wide tolerance on inner angle, dx , and dy with less than a 10% degradation in performance (e.g. using the $kQ_d = 10$ contour in Fig. 7a), indicating flexibility with height constraints and manufacturing tolerances.

Our scalable 2-angle design achieves a simulated Q_d of over 100 at 6.78 MHz, indicating a coil approach worth evaluating. We fabricate these coils to verify the performance and the validity of our simulations.

C. Coil Realization

Additive manufacturing, or 3-D printing, provides a convenient avenue to prototype an arbitrary shape for the coil cross-section. To fabricate the coils, we follow the procedure outlined below and shown visually in Figure 9 (Ref. [52] details a similar process for inductors).

A cross-sectional area (Fig. 9a) is defined with a point-by-point mapping for the inner wall of the simulated structure. Using OpenJSCAD, an online 3D CAD modeling tool, we rotationally extrude this cross-section, leaving a small gap (5–10 mm) for the resonant capacitors and a connector. Our two-dimensional simulations ignore this gap, which we expect to have a minor effect on performance.

This shape is 3-D printed on a plastic scaffold in Formlabs' Form 2 desktop printer (Fig. 9b) and then copper plated by Artcraft Plating (Fig. 9c). Artcraft has a plating tolerance of approximately $5 \mu\text{m}$ for a $50 \mu\text{m}$ copper thickness, and a minimum plating thickness of $0.38 \mu\text{m}$ that far exceeds our minimum plating thickness of 1.25δ at 40.68 MHz, or $15 \mu\text{m}$.

This process can generate arbitrary shapes in a low-cost manner with extremely lightweight coils. At MHz frequencies, the required copper thickness is easily plated with commercial techniques.

TABLE I: Results for simulated and fabricated coils in this project at 6.78 MHz. All dimensions are in mm. Simulated copper thickness is 35 μm , and fabricated copper thickness is 50 μm . Subscript “S” denotes simulations and subscript “M” denotes measured results. kQ_S product is calculated for $g = d/2$. Q_L and R_{EXTRA} are back-calculated from $Q_{T,M}$.

#	Description	d	dx	dy	s _I	s _O	s _T	s _B	Q _{L,S}	kQ _S	Q _{T,M}	Q _L	R _{EXTRA} [m Ω]
1	4-angle	20	1.51	3.94	0.74	0.09	0.06	0.10	219	22.1	107	113	3.7
2	4-angle	40	3.02	7.88	1.48	0.18	0.12	0.21	438	44.2	261	300	1.7
3	2-angle	20	1.28	5.00	0.96	0	0	0	230	22.0	115	122	3.3
4	2-angle	40	2.56	10.00	1.92	0	0	0	448	43.9	282	328	1.3
5	2-angle	60	3.84	15.00	2.88	0	0	0	665	65.8	440	564	0.7
6	2-angle, PCB h	20	2.50	1.60	0.43	0	0	0	87	19.2	88	92	—
7	2-angle, PCB h	60	10.50	1.60	0.39	0	0	0	412	46.0	282	329	1.6
8	6 AWG plated	60	2.91	2.91	90	90	90	90	446	47.4	317	377	1.6

D. Measured Results and Comparisons

Measuring coil quality factor (Q_L) directly is quite challenging with commercial impedance analyzers [42], [54], [55], with expected resistances as low as m Ω s. Because the coils will be used in a WPT resonator, we measure the quality factor of the tank ($Q_{T,M}$ in Table I) and back-calculate the inductor quality factor (Q_L) with a known capacitor quality factor (Q_C) under the assumption that the tank quality factor is simply the parallel combination of Q_L and Q_C (valid if the inductor and capacitor are high Q , which is true here). The tank quality factor is the driver for system efficiency, so the direct measurement of Q_T and back-calculation of Q_L suits the application. With air-core inductors and linear capacitors, the small-signal measurements are extensible to large-signal performance and we do not need a large-signal measurement technique (e.g. [6], [56]) to accurately characterize in-situ performance. Further considerations around tank configuration are discussed in Section III-D.

We use Agilent’s E5061B vector network analyzer to measure the impedance magnitude of the resonant tank, with a single-port reflection method for impedances under 2 k Ω and a two-port series-thru method for maximum impedances above 2 k Ω to maintain 10% or better measurement accuracy [57]. Q_T is determined using the 3 dB method, with:

$$Q_T = \frac{\omega}{\Delta\omega_{3dB}}. \quad (2)$$

Q_L is back-calculated from this measurement and Q_C as:

$$Q_L = \frac{Q_C Q_T}{Q_C - Q_T}. \quad (3)$$

Selecting capacitors for high-frequency, high-power, and high- Q is not trivial [58], [59], and a complete investigation lies outside the scope of this work. Nonetheless, Appendix A includes an evaluation of a number of candidate families, and we select ATC’s 100B and CDE’s Type MC(N) RF mica capacitors. The datasheet Q_C values are then used to back-calculate Q_L from the measured Q_T . For the lower-frequency values, many parallel capacitors are used in the tanks built and measured here; where preferred, a smaller number of higher-value capacitors can be used with the accompanying degradation in Q_C that is shown in Appendix A.

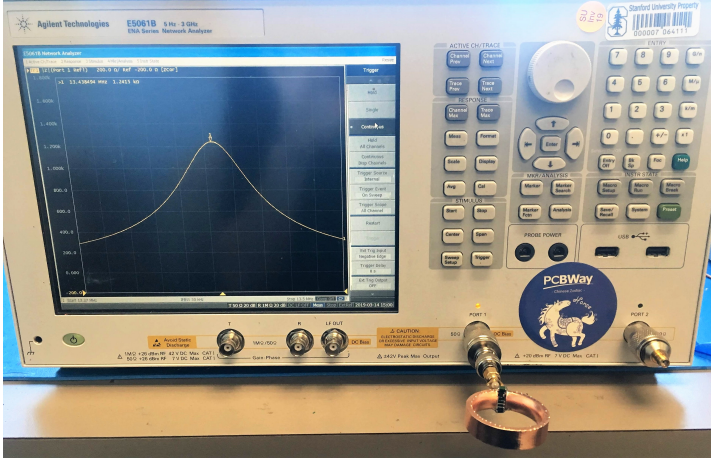
Figure 10 shows both the direct measurement and post-processing to find Q_T for the 2-angle optimized, 4 cm coil.

TABLE II: Measured results for fabricated coils across frequency. Q_L is back-calculated from the tank quality factor, Q_T . 1000 pF, 470 pF, 100 pF, and 33 pF capacitors are Type MC(N) mica series, and all other values are 100B series.

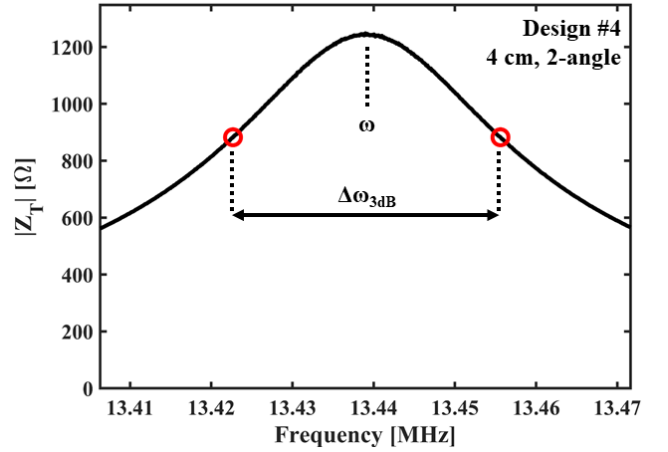
#	f ₀ [MHz]	Capacitors [pF]	L [nH]	Q _T	Q _L
1	6.95	27x 1000	20.3	107	113
	13.73	10x 470	18.3	195	214
	27.05	3x 470, 2x 100, 1x 240	17.8	229	283
	40.66	3x 240, 1x 100	17.2	274	335
2	6.82	14x 1000	38.2	261	300
	13.56	8x 470, 1x 240	37.7	393	478
	27.03	3x 240, 1x 100, 1x 33	38.0	461	583
	40.48	3x 100, 2x 33, 1x 15	38.7	469	613
3	6.95	27x 1000	20.2	115	122
	13.84	10x 470	18.2	195	214
	27.00	4x 470	17.3	245	308
	40.88	3x 240, 2x 33, 1x 12	17.5	259	313
4	6.96	14x 1000	36.6	282	328
	13.44	8x 470	36.2	408	501
	27.18	1x 470, 1x 240, 1x 100, 2x 33	36.9	422	651
	40.87	1x 240, 1x 100, 1x 33	38.6	398	661
5	7.01	9x 1000	55.7	440	564
	13.83	5x 470	54.1	553	739
	27.10	5x 100, 2x 33, 1x 27	56.4	565	760
	40.62	2x 100, 1x 33, 1x 27	56.7	583	823
6	6.61	27x 1000	22.4	88	92
	13.63	9x 470	20.2	143	153
	27.14	3x 470, 4x 100	18.1	203	224
	40.58	2x 240, 3x 100	18.3	230	271
7	6.84	9x 1000	59.6	282	329
	13.82	4x 470, 240, 2x 33	59.0	392	477
	27.06	5x 100, 2x 33	60.6	425	526
	40.43	1x 220, 1x 27	59.6	485	640
8	6.80	6x 1000	90.0	317	377
	13.85	3x 470	91.0	415	511
	27.20	1x 240, 1x 100, 1x 18	90.3	526	691
	40.81	1x 150	89.5	547	861

For each design, the frequency is tuned only within 300 kHz of the center of each ISM band, as the exact tank ω will depend on the application and a small change in resonant frequency will not materially alter Q_T . This measurement is repeated for each coil at all four ISM bands, with the measured Q_T and back-calculated Q_L reported in Tables I and II.

Table I directly compares simulated and measured results at



(a) Single-port reflection $|Z|$ measurement on E5061B.



(b) Matlab post-processing to find ω , 3 dB bandwidth, and Q_T .

Fig. 10: Example measurement for 4 cm, 2-angle coil near 13.56 MHz.

6.78 MHz. With the exception of the lowest- Q coil (Coil #6), the fabricated coils all achieve measured (back-calculated) Q_d around 100 points worse than the simulated Q_L . While this is a large difference in Q , this degradation is accounted for with only 1-4 mΩ extra resistance (R_{EXTRA}). We believe this increase to be a combination of solder interconnects (the largest contribution), eddy currents in the unused copper (discussed in Section III-B), surface roughness from the 3-D printing and plating techniques, and the effect of the gap and SMA connector on the magnetic field.

Even with this extra resistance, the coils achieve excellent performance, with Q_d above 73 cm^{-1} at 6.78 MHz for the resonant tank (Coil #5), well above the state-of-the-art for air-core coils of 42 cm^{-1} [36]. At 13.56 MHz, the best constructed tank achieves a Q_d of 104 cm^{-1} (Coil #4), again significantly outperforming the benchmark of 82 cm^{-1} [36]. At 27.12 MHz and 40.68 MHz, measured maximum Q_d values of respectively 122.5 cm^{-1} (Coil #3) and 137 cm^{-1} (Coil #2) indicate that efficient WPT at higher frequencies may be achievable. Further, we reiterate that we did not build designs with the maximum Q , but instead the maximum kQ product, which is the key parameter for the WPT application. Table II shows Q for each design near the four ISM frequencies, and Q_d is plotted for all of the designs in Figure 11.

III. EXTENSIBILITY OF DESIGN

While the optimized coils appear high-performance, there is little value in a coil that must be optimized as gap, frequency, size constraints, or operating points change. In this Section, we analyze the effects of gap, frequency, and coil size on performance, with particular attention paid to size scaling and if a single coil can be used across frequency and gap without requiring reoptimization.

A. Effect of Diameter and Height

Figure 11 highlights a few key scaling results. At low frequency (6.78 MHz) and small coils, Q_d monotonically increases with taller coils. As the frequency is increased, the

large decrease in Q_C (see Appendix A) results in a decrease of Q_d with increasing coil height, even as absolute Q improves. We see that both height and frequency are knobs to improve Q_d , but must be applied in the correct regions of operation and application. If the design is height-constrained, for example to the PCB height of 1.6 mm, the designer should explore higher-frequency designs to achieve high- Q , and therefore high efficiency, operation. If the design is fixed at 6.78 MHz, taller coils are preferred.

At larger coil sizes (e.g. 6 cm), the effect of a finite Q_C is large, and we no longer achieve a linear increase of Q_d with coil height. Because of the very high Q_L at this size, Q_C starts to drive Q_T , and therefore increasing the frequency beyond 13.56 MHz does not improve performance. As even larger coils are explored, designers must carefully consider capacitor selection and connection techniques.

B. Effect of Frequency

We are explicitly focusing on MHz-range wireless power transfer here. At lower frequencies, litz-wire designs significantly outperform the design approach outlined here. Specifically, Ref. [11] provides analytical approximations for the maximum Q of litz-wire coils in wireless power transfer systems. Figure 12 shows the maximum coil Q_d for ideally-wound litz wire in three of the smallest commercially-available gauges [60]. Even with ideal twisting, the smallest available litz wire barely exceeds this work at 6.78 MHz, and at the higher MHz ISM bands, the measured results outperform idealized litz wire. Additionally, measured resistances at MHz frequencies are much higher than the idealized case due to non-ideal twisting [11], [60].

The variation of frequency has very little effect on the coil design within the achievable MHz ISM bands (beyond 40.68 MHz, the next band is 433.92 MHz). The optimal cross-section shape is constant with varying frequency since the magnetic field shape and coupling do not change with frequency. The primary parameter affected by frequency is skin depth, which will determine the desired thickness of copper

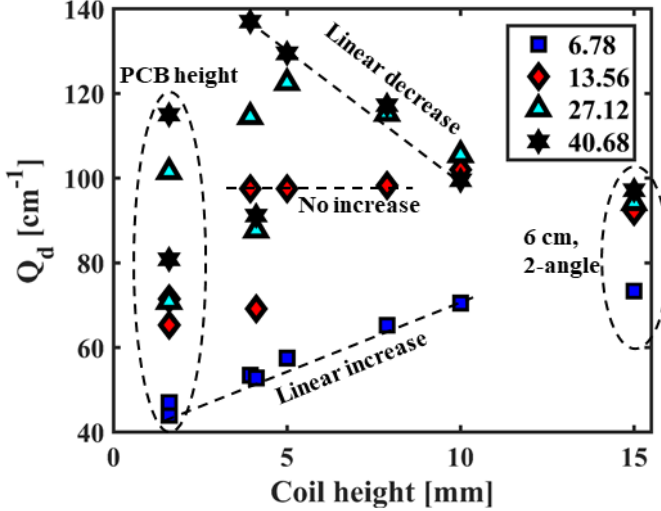


Fig. 11: Measured diameter-normalized resonant tank quality factor, Q_d , across coil height and with changing frequency.

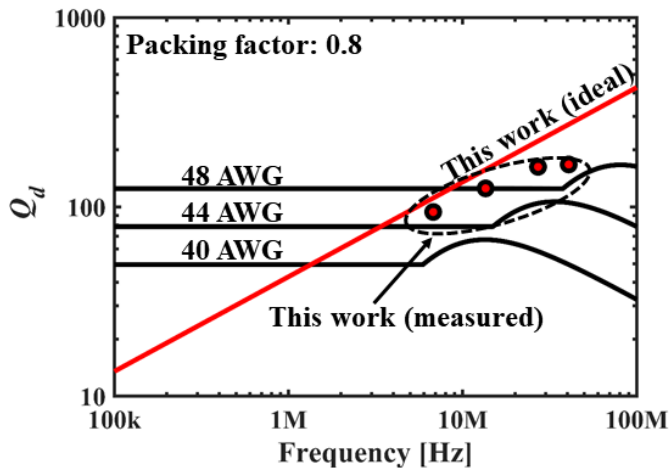


Fig. 12: Comparison in coil quality factor (normalized for diameter) between this work and idealized air-core litz wire coils with an optimistic packing factor, from [11].

plating. Figure 13 shows the variation of the normalized figure-of-merit, kQ_d , with copper thickness, normalized for skin depth. This graph indicates, as expected from known litz wire techniques [5], that the optimal copper thickness is close to 1δ ; for this design, 1.25δ gives the best simulated performance.

Within the achievable MHz ISM bands, there is only a 7.1% degradation in performance from “too thick” of copper plating. This indicates that we can plate our coils with 1.25δ thick copper at 6.78 MHz ($35 \mu\text{m}$) and use the coils across frequency without significant penalty. In practice, $50 \mu\text{m}$ -plated coils outperformed $35 \mu\text{m}$ -plated coils, which may be due to varying thickness in the plating process or surface roughness from 3-D printing. These results indicate that optimizing t_{CU} may marginally improve performance, but our control over the plating and finish processes is not tight enough to merit its inclusion in the optimization process.

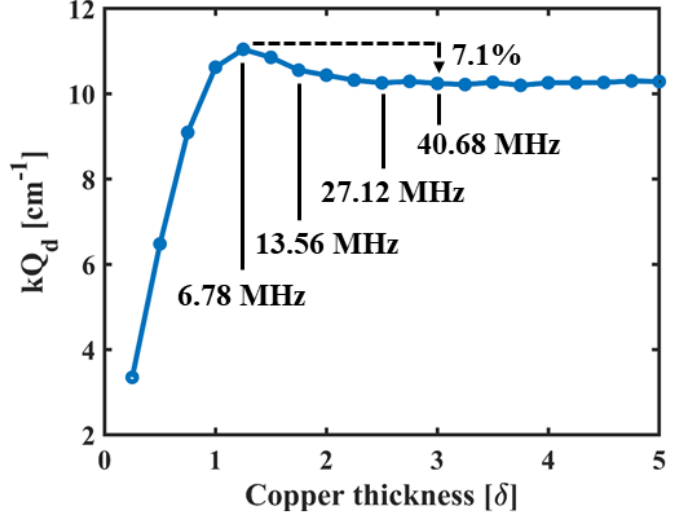


Fig. 13: Effect of copper thickness on simulated kQ for Coil #3 from Table I. Across the achievable MHz-frequency bands, there is only a 7.1% penalty from plating “too thick” of copper.

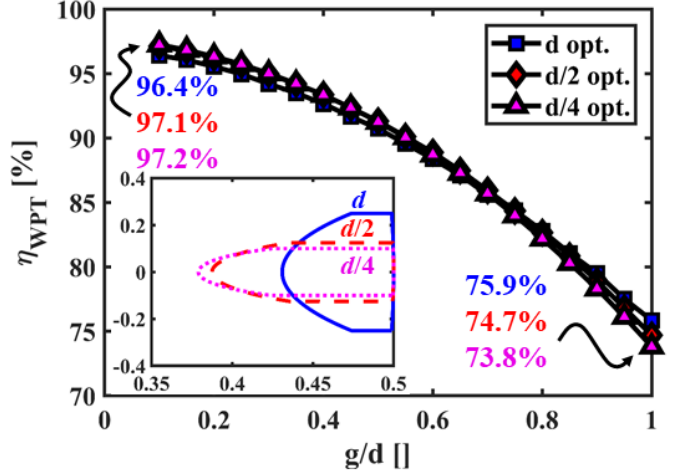


Fig. 14: Simulated WPT link efficiency with varying gap for shapes optimized at three gap distances. Inset graph shows the optimized shapes, with the axes given as ratio of coil diameter.

C. Effect of Gap

For all of the designs in Table I, the design is optimized for the largest kQ product at a gap of the coil radius, $g = d/2$. For most WPT applications, this gap will vary both axially and in the lateral, misaligned plane, and the correct coil optimization may change with the location.

The initial optimization is performed at $d/2$, we repeat optimizations for gaps of d and $d/4$ (for a 2 cm d coil). The optimized coil shape for these results is shown in the inset of Figure 14. At large gaps ($g = d$), the coupling is very weak, the optimization focuses on maximizing Q since varying the shape does not have a large effect on k , and the coil uses the maximum allowable height. At small gaps ($g = d/4$), the opposite is true – coil height significantly impacts coupling, and a short coil is preferred.

For each of these optimized shapes, the link efficiency (Eqn. 1) is plotted across gap variation. As expected, the

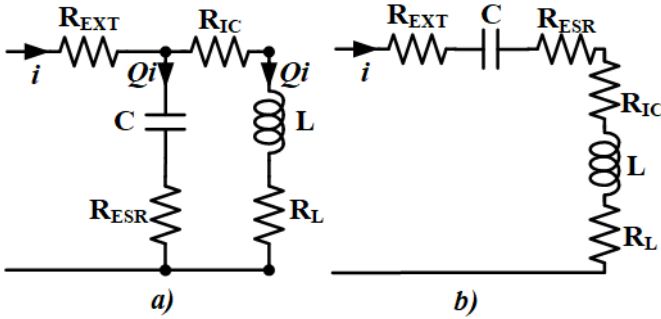


Fig. 15: Unloaded parallel (a) and series (b) resonant circuits, with identical components and the same input rms current, i .

$d/4$ -optimized coil performs best at short range, and the d -optimized coil is preferred at long range. More importantly, the variation between the three coils is very small across the entire range, indicating that a single design may be used for varying gap and misalignment (which has a similar effect on k as axial variation, but may alter the magnetic field shape) with a relatively minor penalty. For a known variation in gap and/or alignment, an optimization can be performed over a weighted average of distance, as is performed in Ref. [43].

D. Effect of Tank Configuration

Resonant tanks may generally be configured in parallel or series configurations, and WPT tanks are no different. MHz-frequency WPT systems predominantly use series-resonant tanks for the transmitter because these can be directly driven with voltage-source topologies with zero-voltage-switching (ZVS) [61], [62]; both series- and parallel-resonant tanks are used on the secondary-side, as current-fed resonant rectifiers are simple to implement [63]. Parallel resonant tanks may also be used on the primary side, as shown in Section IV, which combines a standard voltage-source topology with a (relatively) large impedance to transform the source into current-like (similar to [64], which transforms a voltage source into a current source but drives a series-resonant tank).

For each tank type (shown in Figure 15), we model an external resistance R_{EXT} , which represents a lumped connection to the inverter, rectifier, or impedance analyzer, and R_{IC} , which is the interconnect resistance between the capacitor and inductor, use identical passive components in each tank, and excite each tank with rms current i . For a sinusoidal excitation of a passive network, the tank quality factor is [61]:

$$Q = \omega \frac{\text{Peak Stored Energy}}{\text{Power Dissipated}} \quad (4)$$

The peak energy storage can be written as $L \times (Qi)^2$ (during the cycle time when all of the resonant energy is stored in the inductor), and the power dissipation is the sum of the i^2R losses in the circuit. For the parallel configuration:

$$\begin{aligned} Q &= \omega \frac{L(Qi)^2}{(Qi)^2(R_{ESR} + R_L + R_{IC}) + i^2R_{EXT}} \\ &= \frac{\omega LQ^2}{Q^2(R_{ESR} + R_L + R_{IC}) + R_{EXT}}, \end{aligned} \quad (5)$$

which collapses to the familiar equation $Q = X_L/R$ if R_{EXT} is much smaller than $Q^2(R_L + R_{ESR} + R_{IC})$. In the designs here, all four resistances are on the order of $\text{m}\Omega$ and Q is in the hundreds, so the impact of R_{EXT} on Q_T is negligible. For a parallel tank, the key added resistance is between the capacitor and inductor, R_{IC} .

For the series resonant example, the resistances are straightforwardly combined [61], and the tank Q is:

$$Q = \frac{1}{R_{ESR} + R_L + R_{IC} + R_{EXT}} \sqrt{\frac{L}{C}}. \quad (6)$$

For series designs, a large number of turns is required to ignore the external and interconnect resistances, and with the single-turn designs presented here, these parasitics would directly degrade the Q of the tank and the WPT link efficiency.

This simple analysis shows that, for low-turn-count coils, parallel resonant circuits will report higher quality factors that are more indicative of the component performance rather than the surrounding connections (e.g. see the resonators demonstrated in [65]). Further, higher impedance values are more accurately measured on commercial impedance analyzers. For these reasons, our tanks are configured as parallel resonant. The relative performance in WPT systems of series vs. parallel configurations, however, is application-specific, dependent on the converter topologies used, and requires an exploration beyond the scope of this work (for an overview, see [63]).

E. Effect of Manufacturing Variation

As Figure 5 shows, an optimization is important – we cannot 3-D print an arbitrary shape and expect good performance. Near the optimized shapes given above, however, the performance is not sensitive to variations in manufacturing tolerance.

We have shown that copper thickness has a small effect, on the order of 10% (Fig. 13), as long as the plated thickness is thicker than expected. The surface finish on our designs is standard for low-cost, rapid 3-D prototyping printers, and the irregularities from the supports (see Fig. 9b) appear to have little effect on performance. We assumed the plating thickness is uniform and known; further work could precisely characterize the plating through imaging. Variation in dy , dx , or inner angle, as long as the results are close to the optimized value, again has an effect on the order of around 10% on Q_L (see Fig. 7b).

These coils can be fabricated with simple manufacturing techniques and have low sensitivity to minor variations in parameters.

IV. 6.78 MHZ, 500 W WPT DC-DC SYSTEM

The coils are integrated into a full DC-DC wireless power transfer system operating at 6.78 MHz. In general, coil performance will improve with higher frequencies but the

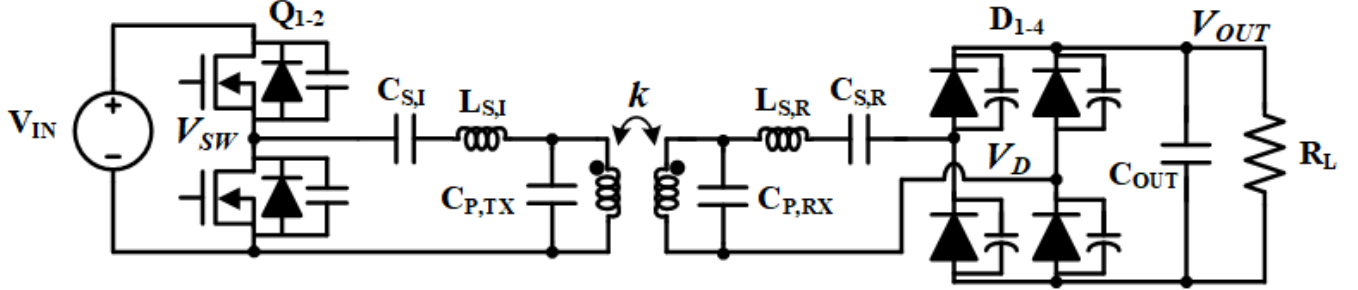


Fig. 16: Simplified schematic for DC-DC wireless power transfer system. All labeled voltages are ground-referenced.

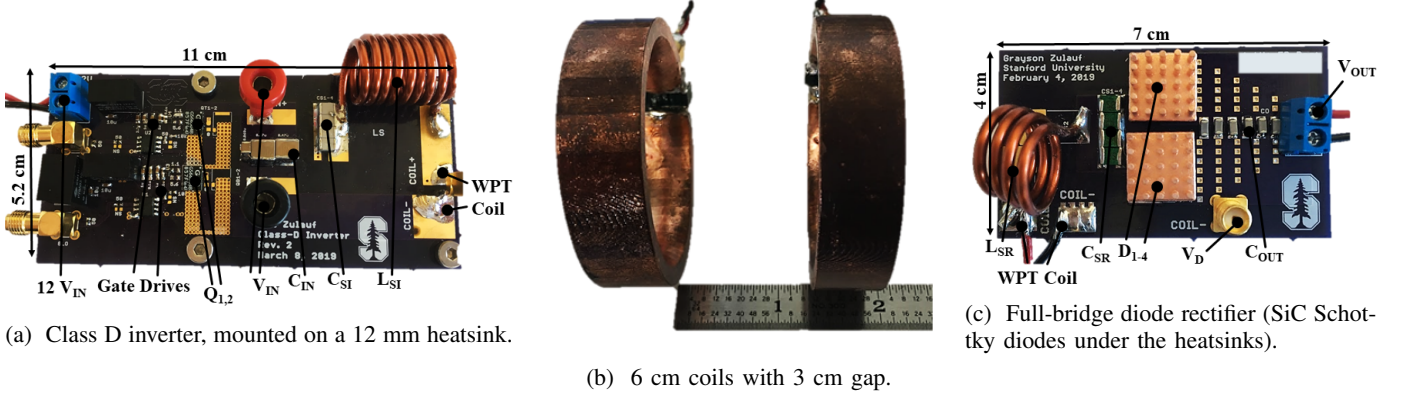


Fig. 17: Implemented inverter (a), WPT resonant tank (b), and rectifier (c) for 6.78 MHz wireless system demonstration.

power electronics efficiency will decrease due to frequency-dependent semiconductor non-idealities [66]. For this demonstration, we utilize a half-bridge Class D inverter with a series tank (to transform the voltage-source to current-like) to drive the parallel-configured coils, and a simple full-bridge rectifier to rectify the WPT receiver output. The Class-D inverter is selected for high efficiency, low semiconductor voltage stress, and low parts count; at higher frequencies or higher powers, where the high-side gate drive is difficult to generate and/or the common-mode dV/dt limits the safe operating envelope, topologies with a single ground-referenced switch such as the Class- Φ_2 [67] or the Class-E [68] may be preferred. These carry the penalty of higher voltage stress, more required inductors, and lower efficiencies but can be operated at much higher frequencies. The powertrain circuit diagram is shown in Figure 16, the critical components for the system are listed in Table III, and the coils and the high-frequency inverter and rectifier boards are shown in Figure 17.

We utilize GaN Systems' GS66504B HEMTs with TI's LMG1020 gate driver for high-speed switching operation. For the high-side driver, an isolated 5 V DC-DC converter is used with the SiLabs 8620 isolator family, and the gate drive signals are inputted from a signal generator.

The combination of the coils, the rectifier, and the L_S-C_S series tanks must provide an efficient drive impedance for the Class-D inverter. This presents a system-wide optimization opportunity that is beyond the scope of this work, but we provide a brief background on the techniques used here.

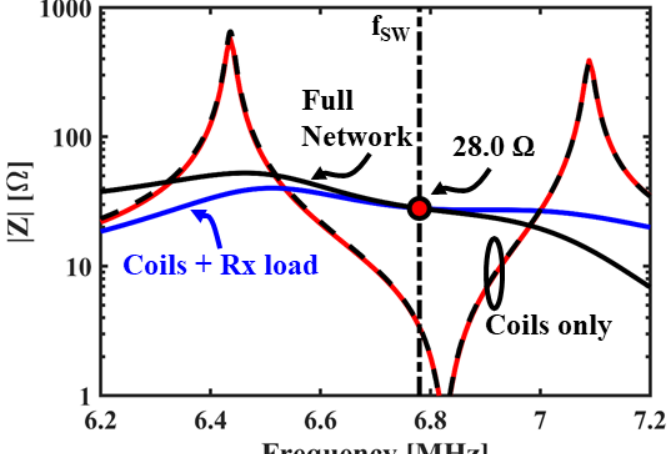
Figure 18 shows the procedure for tuning the network to achieve an efficient phase and magnitude for Class-D inverter

TABLE III: Key components for in DC-DC system demonstration, with identifiers from Fig. 16. Q reported at 6.78 MHz.

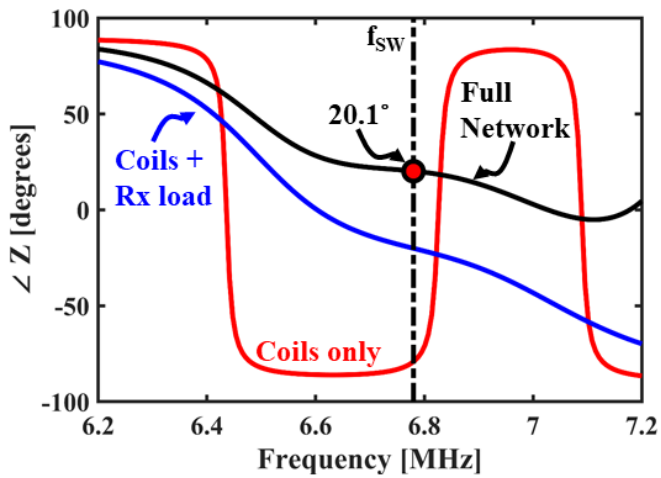
Identifier	Description	Value
C_{IN}	4x 0.47 μ F C2225C474MBRACTU 3x 68 nF C1210C683KDRAC TU	2.084 μ F
$Q_{1,2}$	GS66504B	—
Gate Driver	LMG1020	—
$C_{S,I}$	4x 1 nF 1812SA102JAT1A	4 nF
$L_{S,I}$	Handwound solenoid	566 nH, $Q \approx 300$
$C_{P,TX}$	10x 1000 pF MC22FD102J 1x 470 pF MC18FD471J	10.47 nF
WPT Coils	$d = 6$ cm, $g = 3$ cm	$Q_T = 440$
k	Measured at $g = 3$ cm	0.095
$C_{P,RX}$	10 \times MCN 1000 pF	10 nF
$L_{S,R}$	Handwound solenoid	268 nH, $Q \approx 170$
$C_{S,R}$	4x 470 pF MC18FD471J	1.88 nF
D_{1-4}	2x STPSC406B	—
C_{OUT}	6x 8.2 nF CGJ5L3C0G2D822JA160AA	49.2 nF
R_L	2x 250 W, 50 Ω 58C09860F01	25.2 Ω

operation. Firstly, the previously-discussed 6 cm d coils are selected to achieve high efficiency across a 3 cm gap (g). The receive coil is tuned to resonate near or at the switching frequency (6.78 MHz) and the transmit coil, which has greater influence over the impedance seen by the inverter, is tuned to appear slightly capacitive at the fundamental to a) reduce the impedance variation with coupling and b) provide a lower impedance (than at resonance) to the inverter.

The measured and modeled coil magnitude (open load) are shown in Fig. 18a. Modeling is necessary to ascertain the self-inductances and mutual inductance of the loosely-coupled transformer, all parameters that vary with coupling and are



(a) Network magnitude.



(b) Network phase.

Fig. 18: Procedure for coil tuning, with the modeled magnitude (a) and phase (b) of the coils, coils with receive load, and full network shown. Measured coil magnitude used for k calculation shown overlaid in (a).

not known accurately *a priori*. This empirically-fitted model, which agrees accurately with the measurements, is used to calculate the reported k in Table III and to tune the remainder of the system impedances. With $Q_T = 440$ and the measured k of 0.095, the maximum WPT link efficiency is 95.7%, and we select an output load near the optimal load resistance for these coils [69].

The voltage-mode rectifier impedance is modeled as a parallel resistor-capacitor [3], and, the impedance of the coils with the receive load is shown next in Fig. 18 (“Coils + Rx Load”). This load remains capacitive, and will not result in a zero-voltage-switched (ZVS) inverter.

The L_{SI} - C_{SI} series tank is then designed for three objectives: first, a DC blocking characteristic must be included; second, the impedance must be large enough to transform the voltage-source inverter into current-source-like to drive the resonant tank; lastly, L_{SI} - C_{SI} must provide a positive

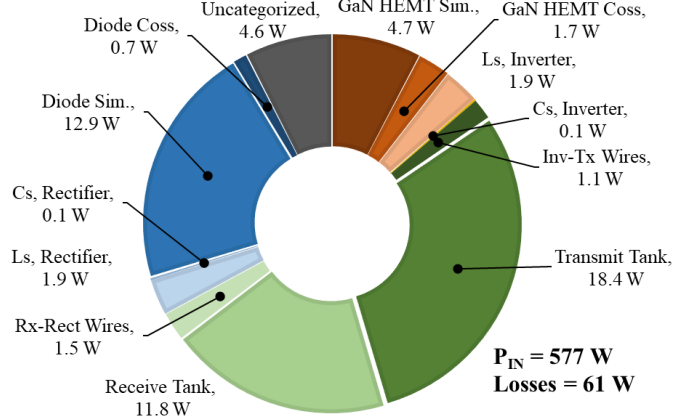


Fig. 19: Calculated distribution of losses at maximum power of $300 V_{IN}$ and 516 W output power.

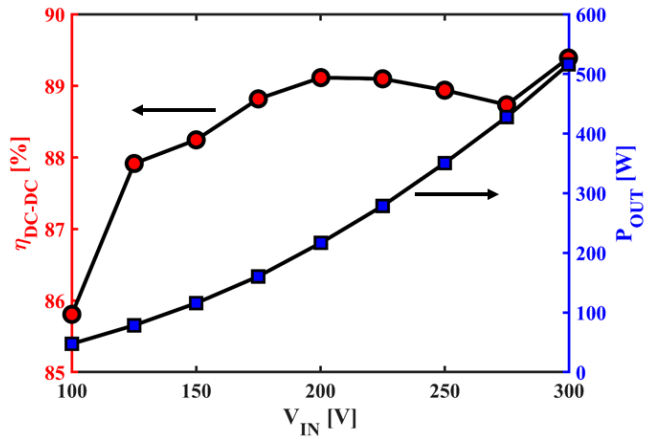


Fig. 20: Measured output power and DC-DC system efficiency, excluding gate drive and fan power of 2.5 W combined. $300 V_{IN}$ value is measured after 3 min. of operation, while other values are measured at thermal steady-state (10 min.).

imaginary impedance to move the impedance seen by the inverter from capacitive to inductive to achieve ZVS. We select a relatively large C_{SI} for DC-blocking, and select an inductor design value of 550 nH to form, in combination with the rest of the passive network, a suitable impedance for Class-D operation in the inverter at the maximum power setpoint. With the L_{SI} - C_{SI} impedance added, the inverter drives a 28Ω , 20° load, an efficient impedance for Class-D operation with the selected semiconductors. The quality factor of the series networks is not as critical to system efficiency as the quality factor of the resonant tank used for WPT, as these components see a current of i while the passive components used for WPT see a much higher current of Qi (see Fig. 15).

Again, these tradeoffs present a system-wide optimization problem, and similar design objectives can, for example, be accomplished with an inductively-tuned transmit coil and a capacitive series tank (with additional third harmonic rejection). Similar arguments as presented above apply to the rectifier L_{SR} - C_{SR} series tank, although the objectives are simplified because the full-bridge provides zero DC-bias and precise impedance tuning is not as critical for the rectifier as for the

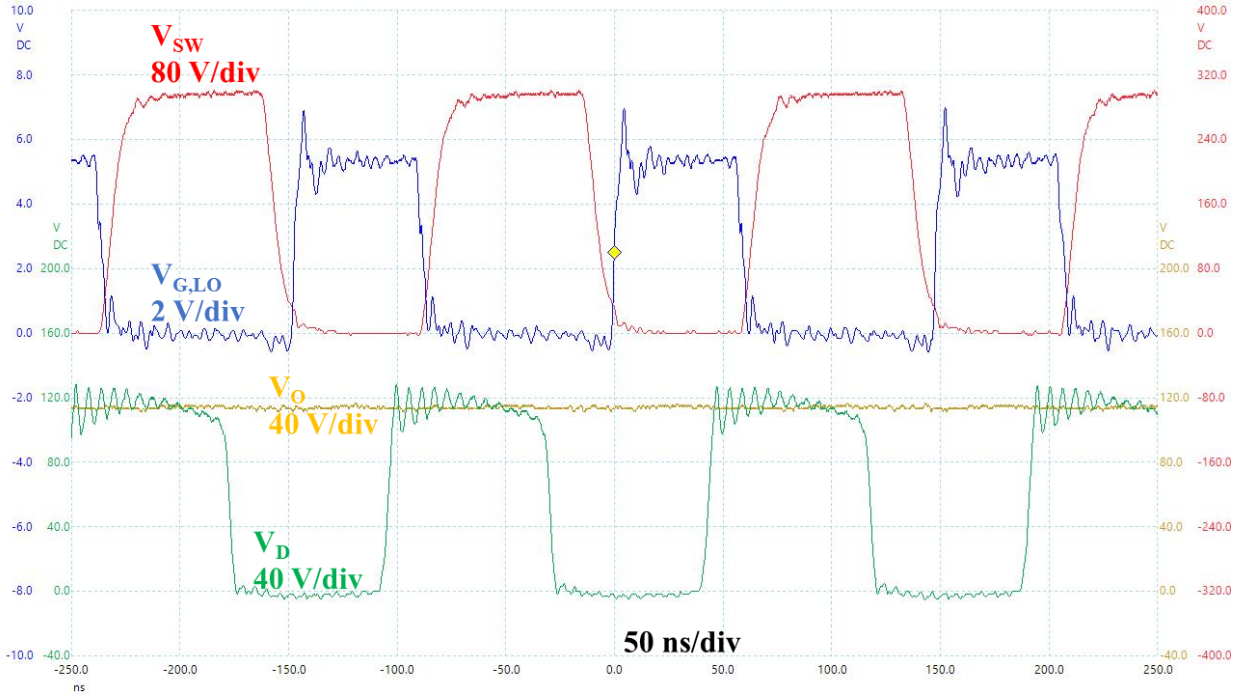


Fig. 21: Measured waveforms (using the PicoScope 6000) for voltages labeled in Figure 16 at $300\text{ }V_{IN}$ and $516\text{ W }P_{OUT}$.

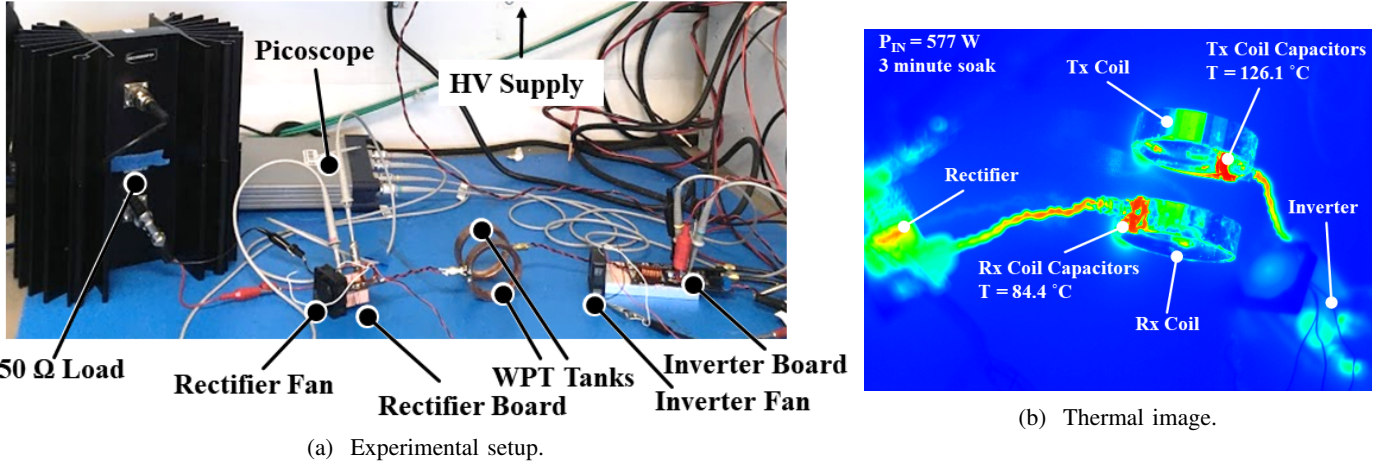


Fig. 22: Experimental setup (HV supply out of the frame) and infrared thermal image of the system at the maximum power setpoint and after 3 minutes of operation. Changes in emissivity between components not considered; infrared image only valid for ballpark thermal characterization. The resonant capacitors limit the power capabilities of the system.

inverter.

The constructed system is tested at input voltages from 100 V to 300 V to vary output power from 50 W to above 500 W under open loop conditions with a constant load resistance. The loss breakdown at maximum output power is shown in Figure 19, the DC-DC system efficiency and output power across input voltage are shown in Figure 20, and the key circuit waveforms at the maximum output power are shown in Figure 21, where we observe near-ZVS of the inverter power devices and a steady output voltage.

The loss breakdown in Fig. 19 is calculated by extracting the losses from the LTSpice simulation model for the wireless power tank (with the previously-measured quality factors), L_S - C_S tanks (with directly measured Q_L), and manufacturer

simulation models for the GaN HEMTs and SiC Schottky diodes. The wires to/from the coils, which contribute over 1 W each, are modeled in the skin depth limit at 6.78 MHz.

Additionally, recent work has shown losses attributable to charging and discharging the semiconductor output capacitor, C_{OSS} , in soft-switched applications, and these “ C_{OSS} losses” must be added to the simulated losses in post-processing. We use Ref. [66] to calculate expected C_{OSS} losses in the GaN HEMTs and Ref. [70] for the SiC Schottky diodes. The reader will note that we utilize 600 V SiC Schottky diodes for an application requiring well under 200 V; we tested a number of more-appropriately-rated 150–200 V Si Schottky diodes in the rectifier, but all performed significantly worse (due to C_{OSS} losses, we suspect) than the 600 V devices.

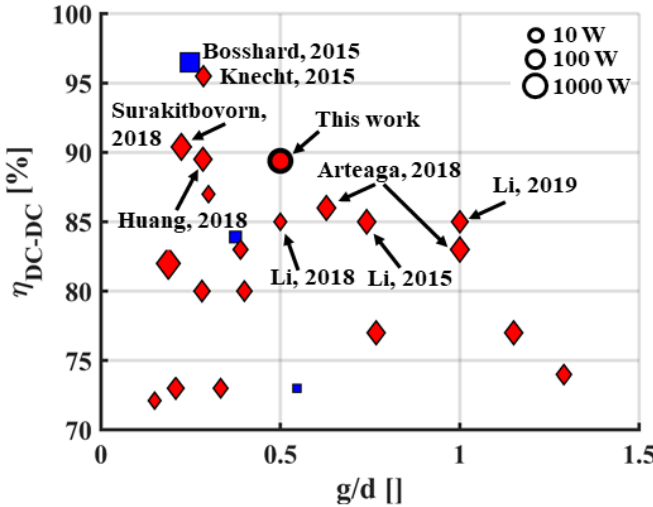


Fig. 23: Wireless power system DC-DC efficiency as a function of gap (g) to coil diameter (d) ratio. Marker size indicates power. Red-fill ‘♦’ (existing literature) and ‘●’ (this work) indicate air-core designs and blue-fill ‘■’ indicates designs using magnetic materials. Highlighted references are [3], [8], [19], [27]–[29], [34], [36], and other plotted points are given in the literature review of Fig. 1.

With the C_{OSS} losses included, the estimated losses are within 1% of the measured losses, with uncategorized losses attributed primarily to dynamic effects in the GaN HEMTs and interconnect resistance at the coils.

Without a core material for the coils, the efficiency curve of the WPT link itself is flat across output power, and the changes in efficiency with power in Fig. 20 are due to the inverter and rectifier efficiencies. Most loosely-coupled WPT designs with a core, however, operate in the linear, complex permeability region of the core materials [71] and will exhibit a similarly-flat efficiency curve for the WPT link itself.

A thermal image at maximum power and the full test setup are shown in Figure 22, and this thermal image and the loss breakdown (Fig. 19) clearly highlight that the wireless link still limits both achievable power and system efficiency, comprising nearly 50% of total losses and with the resonant capacitors limiting power throughput. This further underscores that the selection of capacitors and the L-C connection technique are critical for wireless links.

DC-DC WPT efficiency above 89% at $g = d/2$ and 500 W output power is a significant improvement over the state-of-the-art, where higher DC-DC efficiency is only achieved with designs at much smaller gap to diameter ratios (Figure 23). The DC-DC efficiency can be further improved by adding synchronous rectification to the receiver, where the forward diode drops comprise around 20% of total losses.

V. CONCLUSION

We optimize single-turn air-core coil designs for wireless power transfer using 2-D finite element analysis. These coils significantly outperform the state-of-the-art for air-core coils

at MHz frequencies, and are simple to adapt to a given application with the 3-D printed fabrication technique.

Future work will explore improvements based on the core idea. For electrical performance, the most pressing avenues of exploration are the optimized shape with *a*) a core for field-shaping and shielding, *b*) multiple turns, and *c*) asymmetric transmit and receive coils. We will also explore the unexpected variation at thinner plating and techniques to lower the interconnection resistance. On the mechanical side, the coils could be fabricated with a hollow core to facilitate liquid cooling and make the coils lighter.

Finally, we have demonstrated efficient wireless power transfer systems based on these coils at 6.78 MHz, and hope these coils point towards higher efficiency wireless power designs at MHz frequencies. Even with the improvements here, however, heating of the wireless link still limits the maximum power, and continued improvement is necessary to keep pushing the limits of MHz-frequency WPT. In the hundreds of watts, the demonstrated high-efficiency, MHz-frequency system holds promise for wireless charging of emerging weight-sensitive applications like drones, automated mobile robots, and light electric vehicles.

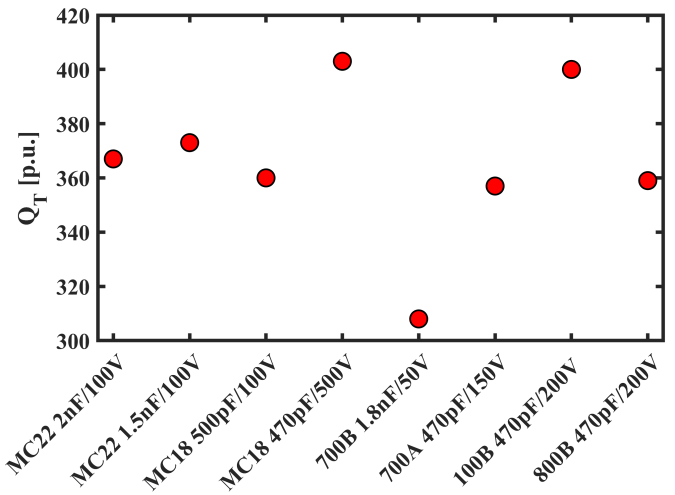


Fig. 24: Measured tank quality factor (Q_T) of 6 cm loop of 6 AWG wire with different capacitors at 13 MHz \pm 1 MHz.

APPENDIX A CAPACITOR SELECTION AND COMPARISON

While a full survey of available high-frequency capacitors is beyond the scope of this work, the part selection is critical to achieving high-Q resonant tanks. These intermediate frequencies pose a particular challenge in deriving information from datasheets, as most power capacitor datasheets give frequency performance up to 1 MHz and most radio-frequency capacitors start above 100 MHz. This section is appended to *a*) provide Q_C for the capacitors used in this work, *b*) show the large variation in Q_C between capacitor families, and *c*) serve as a starting point for capacitor selection for future designers.

We start with families of capacitors with published Q_C in the thousands at the frequencies of interest: ATC’s 100B, 700A, and 800B families and Cornell Dubilier’s Multilayer

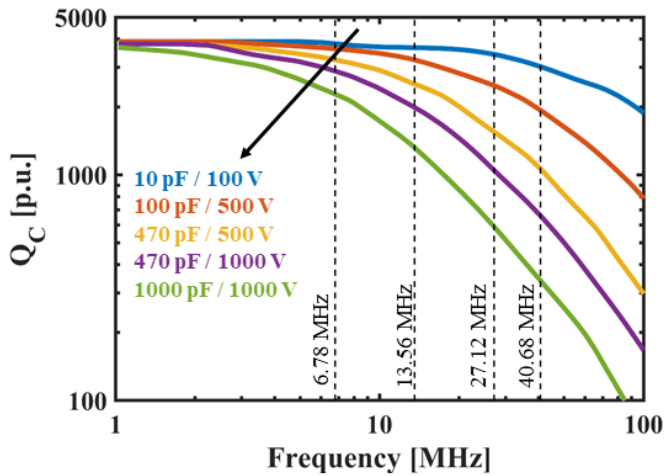


Fig. 25: Type MC and MCN RF mica capacitor quality factor (Q_C), reproduced from [72].

Type MC and MCN RF mica capacitors, and measure the tank quality factor near 13 MHz with a simple 6 cm loop of 6 AWG wire. The results are shown in Figure 24, and we observe large variation in performance between different capacitor families. The MC18 and 100B families achieve the best performance, and these are selected to construct the evaluated tanks.

The Type MC(N) RF mica capacitors are used exclusively for the 6.78 MHz and 13.56 MHz resonant tanks in this work. The Q_C curves from the datasheet are used to back-calculate Q_L from the measured Q_T , and are reproduced in Figure 25. As expected, within a single family we observe a tradeoff of Q_C with *a*) higher voltage rating and *b*) larger capacitance values.

ACKNOWLEDGMENT

We would like to thank Jim Barker and the Arcraft Plating team for expertly and generously plating the 3-D printed coils with copper.

REFERENCES

- [1] Wireless power consortium, Qi certified products. Accessed: 01.11.2019. [Online]. Available: <https://www.wirelesspowerconsortium.com/knowledge-base/testing-and-certification/qi-certified-products.html>
- [2] “Wireless Power Transfer for Light-Duty Plug-In/Electric Vehicles and Alignment Methodology,” Society of Automotive Engineers (SAE) International, USA, Standard, November 2017.
- [3] O. Knecht *et al.*, “High-efficiency transcutaneous energy transfer for implantable mechanical heart support systems,” *IEEE Trans. Power Electronics*, vol. 30, no. 11, pp. 6221–6236, 2015.
- [4] A. Azad *et al.*, “A smart autonomous WPT system for electric wheelchair applications with free-positioning charging feature,” *IEEE Journal of Emerging and Selected Topics in Power Electronics*, 2018.
- [5] C. R. Sullivan. (2016) High-frequency magnetics design: Overview and winding loss. [Online]. Available: <https://www.psma.com/sites/default/files/uploads/tech-forums-magnetics/presentations/high-frequency-magnetics-design-overview-and-winding-loss.pdf>
- [6] A. J. Hanson *et al.*, “Measurements and performance factor comparisons of magnetic materials at high frequency,” *IEEE Trans. Power Electronics*, vol. 31, no. 11, pp. 7909–7925, 2016.
- [7] A. L. Stein *et al.*, “Figure of merit for resonant wireless power transfer,” in *Proc. IEEE Workshop on Control and Modeling for Power Electronics (COMPEL)*, 2017, pp. 1–7.
- [8] R. Bosshard *et al.*, “Modeling and $\eta-\alpha$ -pareto optimization of inductive power transfer coils for electric vehicles,” *IEEE Journal of Emerging and Selected Topics in Power Electronics*, vol. 3, no. 1, pp. 50–64, 2015.
- [9] A. Kurs *et al.*, “Wireless power transfer via strongly coupled magnetic resonances,” *Science*, vol. 317, no. 5834, pp. 83–86, 2007.
- [10] A. L. Stein *et al.*, “Wireless power transfer utilizing a high-Q self-resonant structure,” *IEEE Trans. Power Electronics*, 2018.
- [11] M. Leibl *et al.*, “Inductive power transfer efficiency limit of a flat half-filled disc coil pair,” *IEEE Trans. Power Electronics*, vol. 33, no. 11, pp. 9154–9162, 2018.
- [12] O. Knecht *et al.*, “Optimization of transcutaneous energy transfer coils for high power medical applications,” in *Proc. IEEE Workshop on Control and Modeling for Power Electronics (COMPEL)*, 2014, pp. 1–10.
- [13] E. Waffenschmidt and T. Staring, “Limitation of inductive power transfer for consumer applications,” in *Proc. IEEE European Conference on Power Electronics and Applications (EPE)*, 2009, pp. 1–10.
- [14] A. P. Sample *et al.*, “Analysis, experimental results, and range adaptation of magnetically coupled resonators for wireless power transfer,” *IEEE Trans. Industrial Electronics*, vol. 58, no. 2, pp. 544–554, 2011.
- [15] K. Fotopoulos and B. W. Flynn, “Wireless power transfer in loosely coupled links: Coil misalignment model,” *IEEE Trans. Magnetics*, vol. 47, no. 2, pp. 416–430, 2011.
- [16] C. Florian *et al.*, “Theoretical and numerical design of a wireless power transmission link with GaN-based transmitter and adaptive receiver,” *IEEE Trans. Microwave Theory and Techniques*, vol. 62, no. 4, pp. 931–946, 2014.
- [17] A. Khrapkov *et al.*, “Design of an integrated resonant structure for wireless power transfer and data telemetry,” in *IEEE MTT-S International Microwave Workshop Series on RF and Wireless Technologies for Biomedical and Healthcare Applications*, 2013, pp. 1–3.
- [18] S.-H. Lee and R. D. Lorenz, “Development and validation of model for 95%-efficiency 220-W wireless power transfer over a 30-cm air gap,” *IEEE Trans. Industry Applications*, vol. 47, no. 6, pp. 2495–2504, 2011.
- [19] J. Li and D. Costinett, “Comprehensive design for 6.78 MHz wireless power transfer systems,” in *Proc. IEEE Energy Conversion Congress and Exposition (ECCE)*, 2018, pp. 906–913.
- [20] C. Cheng *et al.*, “Load-independent wireless power transfer system for multiple loads over a long distance,” *IEEE Trans. Power Elec.*, 2018.
- [21] M. Adeeb *et al.*, “An inductive link-based wireless power transfer system for biomedical applications,” *Active and Passive Electronic Components*, vol. 2012, 2012.
- [22] T. Imura *et al.*, “Basic experimental study on helical antennas of wireless power transfer for electric vehicles by using magnetic resonant couplings,” in *Proc. IEEE Vehicle Power and Propulsion Conference*, 2009, pp. 936–940.
- [23] H. Takanashi *et al.*, “A large air gap 3 kW wireless power transfer system for electric vehicles,” in *Proc. IEEE Energy Conversion Congress and Exposition (ECCE)*, 2012, pp. 269–274.
- [24] M. Liu *et al.*, “Low-harmonic-contents and high-efficiency class E full-wave current-driven rectifier for megahertz wireless power transfer systems,” *IEEE Trans. Power Electronics*, vol. 32, no. 2, pp. 1198–1209, 2017.
- [25] M. Fu *et al.*, “Loading and power control for a high-efficiency class E PA-driven megahertz WPT system,” *IEEE Trans. Industrial Electronics*, vol. 63, no. 11, pp. 6867–6876, 2016.
- [26] M. Fu *et al.*, “Analysis and tracking of optimal load in wireless power transfer systems,” *IEEE Trans. Power Electronics*, vol. 30, no. 7, pp. 3952–3963, 2015.
- [27] H. Li *et al.*, “Pulse density modulated ZVS full-bridge converters for wireless power transfer systems,” *IEEE Trans. Power Electronics*, vol. 34, no. 1, pp. 369–377, 2019.
- [28] H. Li *et al.*, “A maximum efficiency point tracking control scheme for wireless power transfer systems using magnetic resonant coupling,” *IEEE Trans. Power Electronics*, vol. 30, no. 7, pp. 3998–4008, 2015.
- [29] Z. Huang *et al.*, “Control design for optimizing efficiency in inductive power transfer systems,” *IEEE Trans. Power Electronics*, vol. 33, no. 5, pp. 4523–4534, 2018.
- [30] H. Li *et al.*, “Pulse density modulation for maximum efficiency point tracking of wireless power transfer systems,” *IEEE Trans. Power Electronics*, vol. 33, no. 6, pp. 5492–5501, 2018.
- [31] X. Tang *et al.*, “Low-cost maximum efficiency tracking method for wireless power transfer systems,” *IEEE Trans. Power Electronics*, vol. 33, no. 6, pp. 5317–5329, 2018.
- [32] W. Zhong and S. Hui, “Maximum energy efficiency operation of series-series resonant wireless power transfer systems using on-off keying

- modulation,” *IEEE Trans. Power Electronics*, vol. 33, no. 4, pp. 3595–3603, 2018.
- [33] K. Surakitbovorn and J. Rivas-Davila, “Design of a GaN-based, inductor-less, wireless power transfer system at 40.68 MHz,” in *Proc. IEEE Workshop on Control and Modeling for Power Electronics (COMPEL)*, 2018, pp. 1–8.
- [34] K. Surakitbovorn and J. Rivas-Davilla, “Design of a GaN-based wireless power transfer system at 13.56 MHz to replace conventional wired connection in a vehicle,” in *Proc. IEEE International Power Electronics Conference (ECCE Asia)*, 2018, pp. 3848–3854.
- [35] T. Dissanayake, “An effective transcutaneous energy transfer (TET) system for artificial hearts,” Ph.D. dissertation, ResearchSpace@ Auckland, 2010.
- [36] J. M. Arteaga *et al.*, “Multi-MHz IPT systems for variable coupling,” *IEEE Trans. Power Electronics*, vol. 33, no. 9, pp. 7744–7758, 2018.
- [37] J. M. Arteaga *et al.*, “A multi-MHz IPT-link developed for load characterisation at highly variable coupling factor,” in *Proc. IEEE Wireless Power Transfer Conference (WPTC)*, 2018, pp. 1–4.
- [38] S. Aldhaher *et al.*, “Light-weight wireless power transfer for mid-air charging of drones,” in *Proc. IEEE European Conference on Antennas and Propagation (EUCAP)*, 2017, pp. 336–340.
- [39] M. Pinuela *et al.*, “Maximizing DC-to-load efficiency for inductive power transfer,” *IEEE Trans. Power Electronics*, vol. 28, no. 5, pp. 2437–2447, 2013.
- [40] B. Wang *et al.*, “Experiments on wireless power transfer with metamaterials,” *Applied Physics Letters*, vol. 98, no. 25, p. 254101, 2011.
- [41] N. Y. Kim *et al.*, “Automated adaptive frequency tracking system for efficient mid-range wireless power transfer via magnetic resonance coupling,” in *Proc. IEEE European Microwave Conference*, 2012, pp. 221–224.
- [42] J. Lawson, “High frequency electromagnetic links for wireless power transfer,” 2017.
- [43] J. M. Arteaga *et al.*, “Dynamic capabilities of Multi-MHz inductive power transfer systems demonstrated with batteryless drones,” *IEEE Trans. Power Electronics*, 2018.
- [44] W. Zhang *et al.*, “Investigation of soft-switching behavior of 600 V cascode GaN HEMT,” in *Proc. IEEE Energy Conversion Congress and Exposition*, 2014, pp. 2865–2872.
- [45] J. Sallán *et al.*, “Optimal design of ICPT systems applied to electric vehicle battery charge,” *IEEE Trans. Industrial Electronics*, vol. 56, no. 6, pp. 2140–2149, 2009.
- [46] C.-J. Chen *et al.*, “A study of loosely coupled coils for wireless power transfer,” *IEEE Trans. Circuits and Systems II: Express Briefs*, vol. 57, no. 7, pp. 536–540, 2010.
- [47] R. Bosshard *et al.*, “Electromagnetic field patterns and energy flux of efficiency optimal inductive power transfer systems,” *Electrical Engineering*, vol. 99, no. 3, pp. 969–977, 2017.
- [48] D. J. Perreault *et al.*, “Opportunities and challenges in very high frequency power conversion,” in *Proc. IEEE Applied Power Elec. Conf. (APEC)*, 2009, pp. 1–14.
- [49] D. Meeker, “Finite element method magnetics,” *FEMM*, vol. 4, p. 32, 2010.
- [50] Mathworks. How globalsearch and multistart work. Accessed: 02.14.2019. [Online]. Available: <https://www.mathworks.com/help/gads/how-globalsearch-and-multistart-work.html>
- [51] C. R. Sullivan *et al.*, “Design and fabrication of low-loss toroidal air-core inductors,” in *Proc. IEEE Power Electronics Specialists Conference (PESC)*, 2007, pp. 1757–1759.
- [52] W. Liang *et al.*, “3-D-printed air-core inductors for high-frequency power converters,” *IEEE Trans. Power Electronics*, vol. 31, no. 1, pp. 52–64, 2015.
- [53] P. N. Murgatroyd, “The optimal form for coreless inductors,” *IEEE Trans. Magnetics*, vol. 25, no. 3, pp. 2670–2677, 1989.
- [54] S. Prabhakaran and C. R. Sullivan, “Impedance-analyzer measurements of high-frequency power passives: Techniques for high power and low impedance,” in *Conference Record of the 37th IAS Annual Meeting of Industry Applications Conference*, vol. 2, 2002, pp. 1360–1367.
- [55] W. Liang *et al.*, “Low mass RF power inverter for cubesat plasma thruster using 3D printed inductors,” in *Proc. IEEE Workshop on Control and Modeling for Power Electronics (COMPEL)*, 2016, pp. 1–7.
- [56] Y. Han *et al.*, “Evaluation of magnetic materials for very high frequency power applications,” *IEEE Trans. Power Electronics*, vol. 27, no. 1, pp. 425–435, 2012.
- [57] Keysight E5061B-3L3/3L4/3L5 LF-RF Network Analyzer with Option 005 Impedance Analysis - Data Sheet, Keysight. [Online]. Available: <http://literature.cdn.keysight.com/litweb/pdf/5990-7033EN.pdf>
- [58] P. A. Kyaw *et al.*, “Power density optimization of resonant tanks using standard capacitors,” in *Proc. IEEE Workshop on Control and Modeling for Power Electronics (COMPEL)*, 2017, pp. 1–7.
- [59] S. Coday *et al.*, “Characterization and modeling of ceramic capacitor losses under large signal operating conditions,” in *Proc. IEEE Control and Modeling for Power Electronics (COMPEL)*, 2018, pp. 1–8.
- [60] C. R. Sullivan and R. Y. Zhang, “Simplified design method for litz wire,” in *Proc. IEEE Applied Power Electronics Conference and Exposition (APEC)*, 2014, pp. 2667–2674.
- [61] R. W. Erickson and D. Maksimovic, *Fundamentals of power electronics*. Springer Science & Bus. Media, 2007.
- [62] M. K. Kazimierczuk and D. Czarkowski, *Resonant power converters*. John Wiley & Sons, 2012.
- [63] O. Knecht and J. W. Kolar, “Comparative evaluation of IPT resonant circuit topologies for wireless power supplies of implantable mechanical circulatory support systems,” in *Proc. IEEE Applied Power Electronics Conference and Exposition (APEC)*, 2017, pp. 3271–3278.
- [64] L. Jiang and D. Costinett, “A high-efficiency GaN-based single-stage 6.78 MHz transmitter for wireless power transfer applications,” *IEEE Trans. Power Electronics*, 2018.
- [65] P. A. Kyaw *et al.*, “High-Q resonator with integrated capacitance for resonant power conversion,” in *Proc. IEEE Applied Power Electronics Conference and Exposition (APEC)*, 2017, pp. 2519–2526.
- [66] G. Zulauf *et al.*, “Coss losses in 600 V GaN power semiconductors in soft-switched, high- and very-high-frequency power converters,” *IEEE Trans. Power Electronics*, vol. 33, no. 12, pp. 10 748–10 763, Dec. 2018.
- [67] J. M. Rivas *et al.*, “A high-frequency resonant inverter topology with low voltage stress,” in *Proc. IEEE Power Elec. Spec. Conf.*, 2007, pp. 2705–2717.
- [68] N. O. Sokal, “Class-E RF power amplifiers,” *QEX*, vol. 204, pp. 9–20, Jan/Feb 2001.
- [69] A. L. Stein *et al.*, “The feasibility of self-resonant structures in wireless power transfer applications,” in *Proc. IEEE PELS Workshop on Emerging Technologies: Wireless Power Transfer (WoW)*, 2018, pp. 1–6.
- [70] Z. Tong *et al.*, “Output capacitance loss characterization of silicon carbide schottky diodes,” *IEEE Journal of Emerging and Selected Topics in Power Electronics*, 2019.
- [71] A. L. Stein *et al.*, “High-Q self-resonant structure for wireless power transfer,” in *Proc. IEEE Applied Power Electronics Conference and Exposition (APEC)*, 2017, pp. 3723–3729.
- [72] Types MC and MCN Multilayer RF Capacitors, Accessed: 02.25.2019. [Online]. Available: <https://www.mouser.com/datasheet/2/88/MC-537734.pdf>